Journal of Materials Chemistry B

PAPER

View Article Online
View Journal | View Issue

Published on 09 April 2014. Downloaded by Florida State University on 21/10/2014 22:57:04.

Cite this: J. Mater. Chem. B, 2014, 2, 4142

Thermo-responsive and shape transformable amphiphilic scaffolds for loading and delivering anticancer drugs†

Smita Kashyap and Manickam Jayakannan*

Shape transformable carriers are an important class of biomaterials for selective drug delivery in a cancer tissue physiological environment. Here, we report the first example of an *in situ* shape transformable thermo-responsive amphiphilic scaffold for loading and delivering anticancer drugs at the cancer tissue temperature. New amphiphiles having a hydrogen bonded amide linkage that connects hydrophilic oligoethylene glycol with the hydrophobic renewable resource 3-pendadecylphenol were tailor made through multi-step organic synthesis. These amphiphiles underwent reversible self-assembly from three dimensional core–shell to rod-like structures in water (or PBS at pH = 7.4). The temperature-induced shape transformation was attributed to the lower critical solution temperature (LCST) and the process was confirmed by light scattering studies, electron microscopy, atomic force microscopy, variable temperature NMR and single crystal structure study. Anticancer drugs such as doxorubicin (DOX) and camptothecin (CPT) were successfully loaded in the core–shell structure without altering the shape transformation ability of the scaffold. *In vitro* drug release studies revealed that the DOX loaded scaffolds showed a selective release of more than 90% of the drug at the cancer tissue temperature (40–43 °C) compared to normal body temperature (37 °C, <10%). The drug kinetics study revealed that the release of DOX at the cancer tissue temperature followed a non-Fickian diffusion process. Thus, the present investigation provides the first insight into the development of *in situ* shape transforming thermo-responsive scaffolds and also establishes the proof-of-concept of their loading and delivering capabilities at the cancer tissue temperature.

Received 23rd January 2014
Accepted 8th April 2014

DOI: 10.1039/c4tb00134f

www.rsc.org/MaterialsB

Introduction

Stimuli-responsive carriers are important biomaterials for delivering anticancer drugs or genes in a controlled manner to a specific site or organ.[1,2] The abnormal cell growth and imperfect lymphatic drainage of cancer tissues accumulates larger sized nano-assemblies (or aggregates of >100 nm size) through an enhanced permeability and the retention (EPR) effect.[3–5] Further, the unusual physiochemical environments of cancer tissues such as a high temperature (40–43 °C)[6,7] and a more acidic environment (pH = 6.1 to 6.8)[8] compared to normal tissues (37 °C and pH = 7.4) has facilitated the development of temperature and pH stimuli drug carriers.[9–11]

Recently, it was understood that apart from size and stimuli the shape of the nano-carriers plays a crucial role in cellular internalization, biodistribution, phagocytosis, and so on.[12,13] It was reported that non-spherical objects like rod-like particles,[14] filo-micelles[15] and elliptical disks[16] with pointed ends were readily internalized by cells compared to spherical objects like micelles and vesicles. Szoka and Frechet proposed a membrane model for the entry of various polymer architectures and concluded that rod-shape carries have a better ability to penetrate the cell membrane.[17] Additionally, the retention of the spherical shape of nano-carriers is very important since they possess a uniform flow behaviour in all three dimensions, which is required for long circulation times, for example in blood plasma during intravenous delivery.[18] This would allow the drug carriers to have both an enhanced transportation and membrane penetration in a single system for maximizing the treatment efficacy. Hence, hypothetically the ideal polymeric or small molecular carriers should retain their three dimensional spherical shape under the normal tissue conditions and should be capable of undergoing *in situ* shape transformation into one dimensional structures in the cancer tissue environment (high temperature or low pH). This concept is schematically shown in Fig. 1.

Thermo-responsive polymers have attracted significant interest in recent years due to their potential application in the

Department of Chemistry, Indian Institute of Science Education and Research (IISER), Dr Homi Bhabha Road, Pune 411008, Maharashtra, India. E-mail: jayakannan@iiserpune.ac.in

† Electronic supplementary information (ESI) available: Guinier plot, crystallographic images, unit cells, DLS data, TCSPC life time table, and ^{1}H-NMR, ^{13}C-NMR, MALDI spectra are provided. CCDC 968254. For ESI and crystallographic data in CIF or other electronic format see DOI: 10.1039/c4tb00134f

This journal is © The Royal Society of Chemistry 2014

Published on 09 April 2014. Downloaded by Florida State University on 21/10/2014 22:57:04.

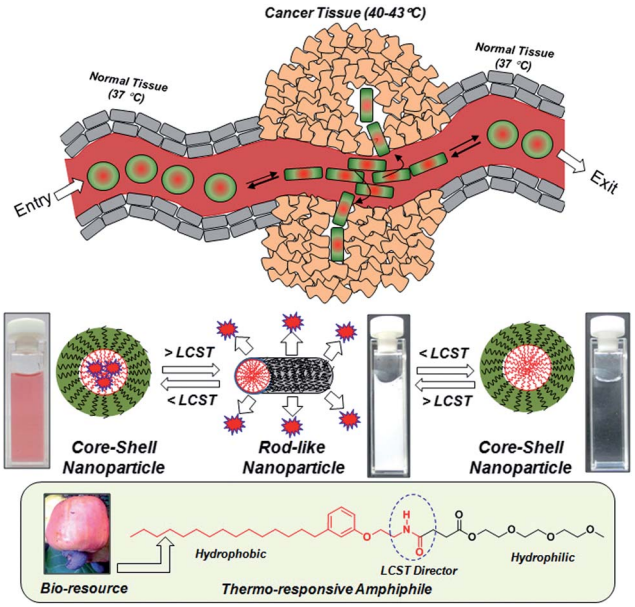

Fig. 1 Schematic representation of shape transformable and thermo-responsive nano-scaffolds in a cancer tissue.

field of drug delivery. These thermo-responsive polymers generally undergo conformational changes in response to a variation in temperature which results in terms of a difference in their solubility in the aqueous medium. The temperature at which this phenomenon occurs is known as the lower critical solution temperature (LCST). Thermo-responsive polymers are ideally expected to retain the loaded cargoes (drugs) at the body temperature (37 °C) and expected to rupture to deliver their load at the cancer tissue temperature (40–43 °C).[19,20] Poly(*N*-isopropyl acrylamide) (PNIPAM) is one the most important thermo-responsive commercial polymers with an LCST at~32 °C. Several attempts were made to modify PNIPAM to adjust the LCST close to the cancer tissue temperature (40–43 °C) so that it could be employed as a drug delivery vehicle. The PNIPAAm-*b*-PMMA diblock copolymer,[21] PMMA-*b*-PNIPAM-*b*-PMMA triblock,[22] PNIPAM–poly(lactic acid) copolymer,[23] PNIPAM-*co*-acrylamide-*b*-poly(caprolactone) random block copolymer[24] and PNIPAM-octadecyl acrylate copolymer[25] are some of the important examples of modified PNIPAMs with an LCST close to or higher than the body or cancer tissue temperature (43 °C). These polymer based micelles were further utilised to encapsulate anticancer drugs like doxorubicin (DOX), anti-inflammatory drugs, and so on. Zhuang and co-workers reported another class of PLG-*g*-PMEO$_i$MA polypeptide with tuneable LCST in the range of 19 to 40 °C for delivering DOX at a low temperature and pH. The same group has also reported pH and reduction responsive PEGylated polypeptide nanogels to successfully deliver doxorubicin (DOX) in the intracellular microenvironment.[26] Though the above literature reports emphasised the need for the thermo-responsive polymers for drug delivery applications, unfortunately, to date there is no reported nano-carrier which could also undergo shape transformations at physiological conditions similar to that of cancer tissues (see Fig. 1). Thus, shape transformable drug carriers with respect to the cancer tissue environment are an important class of biomaterials yet to be developed for the administration of anticancer drugs.

Here, we report the first example of shape tunable thermo-responsive amphiphilic drug carriers and demonstrate the proof-of-concept of their loading and delivering capabilities under the conditions similar to that of cancer tissues. New amide functionalized amphiphiles have been synthesized based on 3-pentadecylphenol, a renewable hydrophobic unit resource, along with oligoethylene glycols as the hydrophilic unit. The amphiphile self-organized into a spherical core–shell nanoparticle at ambient conditions and underwent a morphological transformation into rod-like structures at higher temperatures (above LCST). Single crystal structure, variable temperature NMR studies, light scattering techniques, electron and atomic force microscopies provided evidence for the reversible morphological transformation. Anticancer drugs such as doxorubicin and camptothecin were successfully encapsulated in these thermo-responsive scaffolds. *In vitro* release kinetic studies revealed that the scaffolds were stable at 37 °C in PBS buffer and that they selectively underwent phase transformations at temperatures higher than 42 °C in PBS buffer to release >90% of the loaded cargoes. Thus, the present investigation opens a new area of shape transformable thermo-responsive nano-carriers for loading and delivering anticancer drugs.

Experimental section

Materials

3-Pentadecylphenol, 2-ethanolamine, succinic anhydride, Boc-anhydride triethylamine (Et_3N), triethyleneglycol monomethylether, ethylene glycol monomethylether, diethylene glycol monomethyl ether, 1-ethyl-3-(3-dimethylaminopropyl) carbodiimide (EDC), dicyclohexylcarbodiimide, DIAD (diisopropyl azodicarboxylate), diisopropyl ethylamine (DIPEA), 4-dimethylamino pyridine were purchased from Aldrich chemicals. And all other reagents and solvents were purchased locally and purified following the standard procedure.

General procedures

^{1}H-NMR and ^{13}C-NMR spectra were recorded using a 400 MHz Jeol NMR spectrophotometer in $CDCl_3$ containing a small amount of TMS as the internal standard. Infra-red spectra were recorded using a Thermo-Scientific Nicolet 6700 FT-IR spectrometer in KBr. The mass of all the amphiphiles as well as the intermediate compounds was analysed by an Applied Biosystems 4800 PLUS MALDI TOF/TOF analyser. DLS of the amphiphile was carried out using a Nano ZS-90 apparatus utilizing a 633 nm red laser (at 90° angle) from Malvern instruments. The static light scattering experiment (SLS) was carried out using a 3D-DLS spectrometer, from LS Instruments, Switzerland, utilizing toluene as a reference. The measurement was performed in autocorrelation mode from 30 to 100° by steps of 5°. FE-SEM images were recorded using a Zeiss Ultra Plus

Published on 09 April 2014. Downloaded by Florida State University on 21/10/2014 22:57:04.

scanning electron microscope. For FE-SEM analysis, the samples were prepared by drop casting on silicon wafers and coated with gold. TEM images were recorded using a Technai-300 instrument by drop casting the sample on a Formvar-coated copper grid. Atomic force microscope images were recorded for drop caste samples using JPK instruments attached with Nano wizard-II setup. The reproducibility of the data was checked for at least three independent amphiphile solutions. Single crystals were subjected to data collection at 100 K on a Bruker APEX duo CCD-X-ray diffractometer equipped with a graphite monochromator Mo Kα radiation ($\lambda = 0.71073$ Å). The frames were integrated with the Bruker APEX software package. The structures were solved by direct methods and refined using SHELX S v97 programs. The absorption and emission studies were done by a Perkin-Elmer Lambda 45 UV-Visible spectrophotometer and a SPEX Flurolog HORIBA JOBIN YVON fluorescence spectrophotometer with a 450 W Xe lamp as the excitation source at room temperature. Fluorescence intensity decays were collected by the time correlated single photon counting technique (TCSPC) setup from Horiba Jobin Yvon, using NanoLED-460 for DOX and NanoLED-374 for CPT as the sample excitation sources.

Synthesis of 4-(2-methoxyethoxy)-4-oxobutanoic acid (1a)

Ethylene glycol monomethylether (5.00 g, 65.0 mmol) and succinic anhydride (7.89 g, 78.0 mmol) were dissolved in dry dichloromethane (25 mL) under a N_2 atmosphere. To this reaction mixture, Et_3N (9.15 mL, 65.0 mmol) was added drop wise (**Caution**: the mixtures start to boil vigorously just after the addition of Et_3N). The reaction mixture was then stirred at 25 °C for 24 h under nitrogen. It was poured into water (60 mL) and neutralized with 2 N concentrated HCl (2.0 mL). The organic layer was then washed with brine solution, dried over anhydrous sodium sulphate and was concentrated to obtain a pale yellow liquid as the product. It was purified by passing through a silica gel column with a 60–120 mesh using 5% methanol in chloroform as the eluent. Yield = 8.0 g (69%). ^{1}H-NMR ($CDCl_3$, 400 MHz) δ: 4.24 ppm (t, 2H, CO–OCH_2), 3.60 ppm (t, 2H, CH_2–O), 3.38 ppm (s, 3H, CH_2–OCH_3), 2.66 ppm (s, 4H, CO–CH_2–CH_2). ^{13}C-NMR ($CDCl_3$, 100 MHz) δ: 177.05 (COOH), 171.88 (COO–CH_2), 69.93 (COO–CH_2), 58.51 (C–OCH_3), 28.45 (CO–CH_2–CH_2). FT-IR (cm^{-1}): 3495, 2926, 2852, 1714, 1453, 1406, 1381, 1351, 1198, 1161, 1125, 1096, 1028, 982, 957, 906, 863, 833, 638. MALDI-TOF-MS: *m*/*z* calculated for $C_7H_{12}O_5$: 176.07; and found: 215.03 ($M^+ + K^+$).

Synthesis of 4-(2-(2-methoxyethoxy)ethoxy)-4-oxobutanoic acid (1b)

Diethyleneglycol monomethylether (5.00 g, 42.0 mmol), succinic anhydride (5.00 g, 50.0 mmol) and Et_3N (7.00 mL, 50.0 mmol) were used as given in the procedure for compound **1a**. The product was purified by passing through a silica gel column with a 60–120 mesh using 5% methanol in chloroform as the eluent. Yield = 2.50 g (30%). ^{1}H-NMR ($CDCl_3$, 400 MHz) δ: 4.24 ppm (t, 2H, CO–OCH_2), 3.60 ppm (t, 2H, CH_2–O), 3.38 ppm (s, 3H, CH_2–OCH_3), 2.66 ppm (s, 4H, CO–CH_2–CH_2). ^{13}C-NMR ($CDCl_3$, 100 MHz) δ: 177.05 (COOH), 171.88 (COO–CH_2), 69.93 (OCH_2–CH_2–O), 58.51 (C–OCH_3), 28.45 (COOH–CH_2–CH_2–CO). FT-IR (cm^{-1}): 2923, 1728, 1450, 1351, 1244, 1201, 1162, 1134, 1101, 1028, 934, 839, 625. MALDI-TOF-MS: *m*/*z* calculated for $C_7H_{12}O_5$: 220.22, and found: 259.93 ($M^+ + K^+$).

Synthesis of 12-oxo-2,5,8,11-tetraoxapentadecan-15-oic acid (1c)

Triethyleneglycol monomethylether (10.00 g, 60.0 mmol), succinic anhydride (7.30 g, 73.0 mmol) and Et_3N (8.5 mL, 60.0 mmol) were used as given in the procedure for compound **1a**. The product was purified by passing through a silica gel column with a 60–120 mesh using 10% methanol in chloroform as the eluent. Yield = 10.0 g (62%). ^{1}H-NMR ($CDCl_3$, 400 MHz) δ: 4.14 ppm (t, 2H, CO–OCH_2), 3.60 ppm (t, 2H, CH_2–O), 3.56–3.46 ppm (t, 8H, OCH_2CH_2O), 3.27 ppm (s, 3H, CH_2–OCH_3), 2.54 ppm (s, 4H, CO–CH_2–CH_2). ^{13}C-NMR ($CDCl_3$, 100 MHz) δ: 177.05 (COOH), 171.88 (COO–CH_2), 70.56 (OCH_2–CH_2–O), 69.93 (COO–CH_2), 58.51 (C–OCH_3), 28.45 (CO–CH_2–CH_2). FT-IR (cm^{-1}): 3471, 2881, 2933, 1792, 1453, 1392, 1349, 1244, 1199, 1094, 1026, 941, 846, 751, 666, 622. MALDI-TOF-MS: *m*/*z* calculated for $C_7H_{15}NO_3$: 264.12, and found: 287.04 ($M^+ + Na^+$).

Synthesis of *tert*-butyl (2-hydroxyethyl)carbamate (2)

Ethanolamine (10.00 g, 164.0 mmol) was added to the mixture of 10% Na_2CO_3 (60 mL) and THF (5 mL) and stirred at 25 °C for 10 minutes. Boc-anhydride (42.0 g, 196.0 mmol) in THF (40 mL) was added drop wise in the reaction mixture. After the addition, the content was stirred at 25 °C for 12 h. At the end of the reaction, a white color precipitate was observed. THF was removed by a rota evaporator and the content was extracted with ethyl acetate (60 mL). The organic layer was neutralized with 5% HCl (40 mL), dried over anhydrous sodium sulphate and the solvent was removed to obtain a colorless liquid as the product. It was purified by passing through a silica gel column with a 60–120 mesh using 10% methanol in chloroform as the eluent. Yield = 23.0 g (88%). ^{1}H-NMR ($CDCl_3$, 400 MHz) δ: 3.64 ppm (t, 2H, CH_2–OH), 3.23 ppm (t, 2H, CH_2–NH), 1.41 ppm (s, 9H, OC–$(CH_3)_3$, 5.25 ppm (s, 1H, CH_2–NH). ^{13}C-NMR ($CDCl_3$, 100 MHz) δ: 156.84 (COO), 79.65 (OC–CH_3), 62.48 (CH_2–OH), 43.09 (CH_2–NH), 28.33 (OC–CH_3). FT-IR (cm^{-1}): 3352, 2976, 2933, 2881, 1683, 1518, 1453, 1393, 1365, 1274, 1249, 1164, 1064, 999, 972, 900, 862, 781, 650. MALDI-TOF-MS: *m*/*z* calculated for $C_7H_{15}NO_3$: 161.11, and found: 184.03 ($M^+ + Na^+$).

Synthesis of *tert*-butyl (2-(3-pentadecylphenoxy)ethyl) carbamate (3) PDP–NH–Boc

Compound **2** (2.64 g, 16.0 mmol), 3-pentadecylphenol (5.00 g, 16.0 mmol) and triphenylphosphine (4.30 g, 16.0 mmol) were dissolved in dry tetrahydrofuran (20 mL). The reaction mixture was then kept in an ice-cooled bath for 10 minutes under a N_2 purge. Diisopropyl azodicarboxylate (3.65 mL, 18.0 mmol) was added drop wise and the reaction mixture was stirred at 25 °C for 24 h. The mixture was directly loaded in a silica gel column with a 60–120 mesh and was eluted using 1% ethyl acetate in hexane as the eluent. Yield = 4.2 g (58%). ^{1}H-NMR ($CDCl_3$,

 This journal is © The Royal Society of Chemistry 2014

Published on 09 April 2014. Downloaded by Florida State University on 21/10/2014 22:57:04.

400 MHz) δ: 7.19 ppm (t, 1H, Ar-H), 6.80–6.70 ppm (m, 3H, Ar-H), 5.02 ppm (s, 1H, NH), 4.02 ppm (t, 2H, Ar-OCH_2), 3.54 ppm (t, 2H, CH_2–N), 2.58 ppm (t, 2H, Ar-CH_2), 1.46 ppm (s, 9H, OC–$C(CH_3)_3$, 1.6–0.88 ppm (m, 29H, aliphatic H). ^{13}C-NMR ($CDCl_3$, 100 MHz) δ: 158.62 (Ar-C), 155.98 (CO–O), 144.85, 129.29, 121.32, 114.75, 111.40 (Ar-C), 79.57 $OC(CH_3)_3$, 67.08 (Ar-OCH_2), 40.26 (CH_2–N), 36.09, 32.00, 29.76, 26.47, 22.77, 14.20. FT-IR (cm^{-1}): 3396, 2916, 2850, 1690, 1590, 1512, 1453, 1362, 1250, 1157, 1060, 959, 866, 778, 690. MALDI-TOF-MS: *m*/*z* calculated for $C_{28}H_{49}NO_3$: 447.37, and found: 470.29 ($M^+ + Na^+$).

Synthesis of 2-(2-(2-methoxyethoxy)ethoxy)ethyl 4-oxo-4-((2-(3-pentadecylphenoxy)ethyl)amino)butanoate (PDP–TEG)

Trifluoroacetic acid (10 mL, 134.2 mmol) was added drop wise to compound **3** (2.00 g, 4.5 mmol) in dichloromethane (5 mL). After stirring the reaction mixture for 1 h at 25 °C the solvent was removed by a rotavapour. Fresh dichloromethane (5 mL) was added to the product and washing was repeated for 3 times to remove TFA. The content was poured in ice-cooled diethyl ether (15 mL). The white solid mass (2.00 g, 5.7 mmol) obtained was dissolved in dry dichloromethane (15 mL) and purged with nitrogen for 15 minutes. To this reaction mixture, **1c** (1.52 g, 5.7 mmol) was added and the content was purged under nitrogen for 15 minutes. EDC (1.32 g, 6.9 mmol) and diisopropylethylamine (2.0 mL, 11.5 mmol) was added to the reaction mixture under nitrogen atmosphere and the reaction was continued for 24 h at 25 °C. The mixture was poured into water (30 mL) and extracted with chloroform (20 mL). The organic layer obtained was neutralized with 2 N HCl (2 mL), washed with aqueous 5% $NaHCO_3$ (50 mL) and brine. After drying over anhydrous sodium sulphate, the solvent was removed to obtain a yellow liquid as the product. It was further purified by passing through a silica gel column with a 60–120 mesh using 25% methanol in chloroform as the eluent. Yield = 2.5 g (78.0%). ^{1}H-NMR ($CDCl_3$, 400 MHz) δ: 7.18 ppm (t, 1H, Ar-H), 6.80–6.69 ppm (m, 3H, Ar-H), 6.26 (CO–NH), 4.24 ppm (t, 2H, COO–CH_2), 4.02 ppm (t, 2H, Ar-OCH_2), 3.69–3.63 ppm (m, 10H, O–CH_2–CH_2), 3.56 ppm (t, 2H, CH_2–N), 2.70 ppm (t, 2H, Ar-CH_2), 3.38 ppm (s, 3H, CH_2–OCH_3), 2.57 ppm (t, 2H, NH–CO–CH_2), 2.51 ppm (t, 2H, CH_2–COO), 1.6–0.88 ppm (m, 29H, aliphatic H). ^{13}C-NMR ($CDCl_3$, 100 MHz) δ: 172.75 (NH–CO), 171.52 (CO–O), 158.42, 144.74, 129.20, 121.27, 114.58, 111.32 (Ar-C), 71.85 (CH_2–OCH_3), 70.48 (O–CH_2–CH_2), 68.92, 66.52 (Ar-OCH_2), 63.70 (COO–CH_2), 58.96 (O–CH_3), 39.05 (CH_2–N), 35.97, 31.87, 31.38, 29.64, 29.32, 22.64, 14.08. FT-IR (cm^{-1}): 3309, 2848, 2915, 1741, 1640, 1552, 1454, 1405, 1351, 1293, 1249, 1203, 1166, 1106, 1045, 952, 857, 777, 696. MALDI-TOF-MS: *m*/*z* calculated for $C_{34}H_{59}NO_7$: 593.43, and found: 616.35 ($M^+ + Na^+$).

Synthesis of 2-methoxyethyl 4-oxo-4-((2-(3-pentadecylphenoxy)ethyl)amino)butanoate (PDP–EG)

Compound **3** (2.00 g, 4.5 mmol), trifluoroacetic acid (10 mL, 134.2 mmol), **1a** (0.50 g, 2.8 mmol), EDC (0.59 g, 2.2 mmol) and diisopropylethylamine (0.98 mL, 5.7 mmol) were used. The product was purified by passing through a silica gel column with a 60–120 mesh using 70% ethyl acetate in pet ether as the eluent. Yield = 0.6 g (42.0%). ^{1}H-NMR ($CDCl_3$, 400 MHz) δ: 7.19 ppm (t, 1H, Ar-H), 6.80–6.69 ppm (m, 3H, Ar-H), 6.13 ppm (CO–NH), 4.24 ppm (t, 2H, COO–CH_2), 4.02 ppm (t, 2H, Ar-OCH_2), 3.67 ppm (t, 2H, CH_2–OCH_3), 3.56 ppm (t, 2H, CH_2–N), 3.38 ppm (s, 3H, CH_2–OCH_3), 2.73 ppm (t, 2H, Ar-CH_2), 2.57 ppm (t, 2H, NH–CO–CH_2), 2.52 ppm (t, 2H, CH_2–COO), 1.6–0.88 ppm (m, 29H, aliphatic H). ^{13}C-NMR ($CDCl_3$, 100 MHz) δ: 172.95 (NH–CO), 171.52 (CO–O), 158.52, 144.89, 129.33, 121.43, 114.71, 111.45 (Ar-C), 70.42 (Ar-OCH_2), 66.66 (CH_2–OCH_3), 63.79 (COO–CH_2), 59.07 (O–CH_3), 39.16 (CH_2–N), 36.10, 32.00, 31.51, 31.07, 29.64, 29.77, 22.77, 14.21 (aliphatic C). FT-IR (cm^{-1}): 3318, 2845, 2915, 1731, 1647, 1542, 1449, 1406, 1351, 1256, 1179, 1124, 1042, 982, 925, 761, 724, 690. MALDI-TOF-MS: *m*/*z* calculated for $C_{30}H_{51}NO_5$: 505.38 and found: 528.37 ($M^+ + Na^+$).

Synthesis of 2-(2-methoxyethoxy)ethyl 4-oxo-4-((2-(3-pentadecylphenoxy)ethyl)amino)butanoate (PDP–DEG)

Compound **3** (2.00 g, 4.5 mmol) and trifluoroacetic acid (10 mL, 134.2 mmol) was added drop wise and **1b** (1.20 g, 5.5 mmol), DCC (1.35 g, 6.5 mmol) and DMAP (0.07 g, 0.6 mmol) were used. The product was purified by passing through a silica gel column with a 60–120 mesh using 50% ethyl acetate in pet ether as the eluent. Yield = 1.2 g (40.0%). ^{1}H-NMR ($CDCl_3$, 400 MHz) δ: 7.19 ppm (t, 1H, Ar-H), 6.81–6.70 ppm (m, 3H, Ar-H), 6.18 ppm (CO–NH), 4.24 ppm (t, 2H, COO–CH_2), 4.03 ppm (t, 2H, Ar-OCH_2), 3.70–3.63 ppm (m, 6H, OCH_2CH_2O), 3.56 ppm (t, 2H, CH_2–N), 3.39 ppm (s, 3H, CH_2–OCH_3), 2.70 ppm (t, 2H, Ar-CH_2), 2.57 ppm (t, 2H, NH–CO–CH_2), 2.51 ppm (t, 2H, CH_2–COO), 1.6–0.88 ppm (m, 29H, aliphatic H). ^{13}C-NMR ($CDCl_3$, 100 MHz) δ: 172.88 (NH–CO), 171.61 (CO–O), 158.54, 144.86, 129.31, 121.40, 114.71, 111.46 (Ar-C), 71.93 (CH_2–OCH_3), 70.50 (Ar-OCH_2), 69.10, 66.65 (CH_2–OCH_2), 63.81 (COO–CH_2), 59.11 (O–CH_3), 39.16 (CH_2–N), 36.09, 31.99, 31.49, 29.75, 29.67, 22.76, 14.19 (aliphatic C). FT-IR (cm^{-1}): 3306, 2848, 2913, 1739, 1639, 1551, 1454, 1402, 1348, 1250, 1203, 1134, 1047, 961, 863, 757, 713. MALDI-TOF-MS: *m*/*z* calculated for $C_{30}H_{51}NO_5$: 549.40 and found: 572.32 ($M^+ + Na^+$). Similarly, two other amphiphiles, DD–TEG and CAR–TEG, were also synthesized and their details are given in the ESI.†

Optical transmittance measurement

Optical transmittance of the amphiphile and drug loaded nanoparticles was measured using a quartz cell (path length: 1 cm) with s Perkin-Elmer Lambda 45 UV-Visible spectrophotometer which was equipped with a temperature-controller. The sample was heated from 30 °C to 80 °C in a stepwise manner with an interval of 5 °C. Similarly, a cooling cycle was recorded from 80 °C to 30 °C with an interval of 5 °C.

Doxorubicin and CPT encapsulation

The ability of these core–shell nanoparticles to encapsulate hydrophobic molecules in the hydrophobic inner core was determined by using DOX. DOX·HCl (0.5 mg) was neutralized with triethylamine prior to the encapsulation. DOX (0.5 mg) and PDP–TEG (5.0 mg) were added to DMSO (1.0 mL). To it triethylamine (1.5 equivalents to DOX) and water (3.0 mL) were added and stirred at 25 °C for 12 h. It was then extensively dialyzed

Published on 09 April 2014. Downloaded by Florida State University on 21/10/2014 22:57:04.

(SPECTRA/POR, MWCO-500-1000) against deionized water (200 mL) for 48 h. The DOX encapsulated solution was filtered through a 0.45 μm filter and the sample was freeze-dried in a lyophilizer.

CPT was encapsulated as described. PDP–TEG (10.0 mg) and CPT (1.0 mg) were dissolved in 2.0 mL of DMSO and stirred for 15 minutes at 25 °C. Water (5.0 mL) was added to the above solution drop wise and the mixture was further stirred for 12 h. It was transferred to a dialysis bag (SPECTRA/POR, MWCO-500-1000) and dialyzed against deionized water (200 mL) for 48 h. The CPT encapsulated solution was filtered through a 0.45 μm filter and the sample was freeze-dried in a lyophilizer. Drug loading efficiency (DLE) and drug loading content (DLC) were calculated using the following equations:[17]

$$\text{DLE (\%)} = \{\text{weight of encapsulated CPT/weight of CPT in feed}\} \times 100\%.$$

$$\text{DLC (\%)} = \{\text{weight of CPT in nanoparticles/weight of CPT loaded nanoparticles}\} \times 100\%.$$

For the above purpose, approximately 1.5 mg of drug loaded nanoparticles were dissolved in DMSO (2.0 mL) and their absorbance was measured to determine the DLE and DLC using their molar extinction coefficients {ε_{CPT} = 10 500 (in PBS), ε_{CPT} = 11 250 (in DMSO) and ε_{DOx} = 4188 (in PBS), ε_{DOx} = 7035 (in DMF)}.

In vitro drug release studies

The release profile of DOX was studied using the dialysis method. Briefly, 3.0 mg of drug loaded sample was dispersed in 3.0 mL of PBS and the content was transferred into a dialysis bag, which was then immersed in 100 mL of PBS and was incubated at 37 °C. Periodically, 3.0 mL of solution was withdrawn from the system and was replaced with 3.0 mL of fresh PBS solution. The aliquots obtained were then subjected to absorbance measurements and the amount of DOX released was calculated. The release profile of DOX was also studied at 25 °C and 44 °C. Similarly, 3.0 mg of CPT loaded nanoparticles were subjected to *in vitro* release studies at 25 °C, 37 °C and 55 °C.

Results and discussions

Synthesis and thermo-responsiveness of amphiphiles

The synthesis of amphiphilic molecules from commercially available ethylene glycols as the hydrophilic part and the renewable resource 3-pentadecylphenol (PDP) as the hydrophobic part is shown in Scheme 1. Briefly, succinic anhydride was ring opened with oligoethylene glycol monomethyl ether derivatives $CH_3O(CH_2CH_2)_xOH$, where x = 1, 2 and 3 in presence of Et_3N to give acids **1a–1c**. Ethanolamine was reacted with Boc-anhydride to give *tert*-butyl (2-hydroxyethyl) carbamate (**2**). Compound **2** was reacted with PDP under Mitsunobu coupling reaction in the presence of triphenylphosphine and diisopropyl azodicarboxylate to give *tert*-butyl (2-(3-pentadecy-8-en-1-yl)-phenoxy)ethyl carbamate (**3**). Compound **3** was further hydrolysed by trifluoroacetic acid (TFA) and coupled with **1a–1c** to give the amphiphiles. These amphiphiles are named PDP–X, where X = EG, DEG, and TEG with respect to the number of $(CH_2CH_2)_xO$ units x = 1, 2, and 3, respectively. Two more amphiphiles based on cardanol (CAR, have unsaturated double bonds in the C15 alkyl tail) and dodecyl amine (DD) (see structures in Scheme 1) were also prepared and their details are given in the ESI (see SS-1).†

The structures of the amphiphiles were characterized by ^1H, ^{13}C-NMR, and MALDI-TOF (see the ESI†). The solubility of the amphiphiles in water was found to be dictated by the number of the ethyleneoxy units rather than the hydrophobic units (PDP, CAR or DD). For example, the amphiphiles with very short $(CH_2CH_2O)_x$ units, PDP–EG and PDP–DEG, were found to be completely insoluble in water (thus, these two short amphiphiles were not included in any further studies). On the other hand, the other three amphiphiles, PDP–TEG, CAR–TEG and DD–TEG, were found to be dispersible in water or PBS buffer (pH = 7.4) at 25 °C.

To study the thermo-responsive behaviours of the amphiphiles, they were subjected to optical transmittance measurements as a function of temperature using absorption spectroscopy. The plot of the optical transmittance of PDP–TEG is shown in Fig. 2a. The plot consists of data from two consecutive heating and cooling cycles from 30 °C to 80 °C. The plots reveal that the optical transmittance was 90% below 40 °C (solution was clear) and the sample became opaque and turbid above 42 °C (<50% transmittance). The vials in the photographs clearly show the change in the transmittance in the heating and cooling cycles. Further, the plots also revealed that the formation and clearance of turbidity in the heating and cooling cycles, respectively, follow different kinetic paths. For example, in the heating cycle, the appearance of turbidity began at 40 °C and slowly completed itself at 70 °C. On the other hand, in the cooling cycle the change from a turbid to a clear solution occurred sharply at 45 °C. This suggested that self-assembly was a slow process in the heating cycle whereas the reversibility was very sharp in the subsequent cooling. Thus, the lower critical solution temperature (LCST) of the PDP–TEG was assigned as 42 °C.

The thermo-responsive nature of PDP–TEG at a concentration ranging from 1×10^{-5} to 1×10^{-3} M was investigated and the cooling cycle data are shown in Fig. 2b (see Fig. S1 for their heating cycle data†). The LCST of PDP–TEG decreased with an increasing amphiphile concentration. At very low concentrations, PDP–TEG did not show any phase-separation phenomena. This indicated that the LCST of the amphiphile was a concentration driven process. Further, the complete reversibility of the thermo-responsive behaviour of the amphiphiles was studied by measuring the optical transmittance of the amphiphiles both at temperatures above and below LCST for ten consecutive cycles. And it was observed that the thermal response of the amphiphiles was completely reversible (see Fig. S2†). The cloud points obtained for each concentration were plotted and are shown in Fig. 2c. The plot reveals that LCST varied linearly with the concentration of the amphiphile

 This journal is © The Royal Society of Chemistry 2014

Published on 09 April 2014. Downloaded by Florida State University on 21/10/2014 22:57:04.

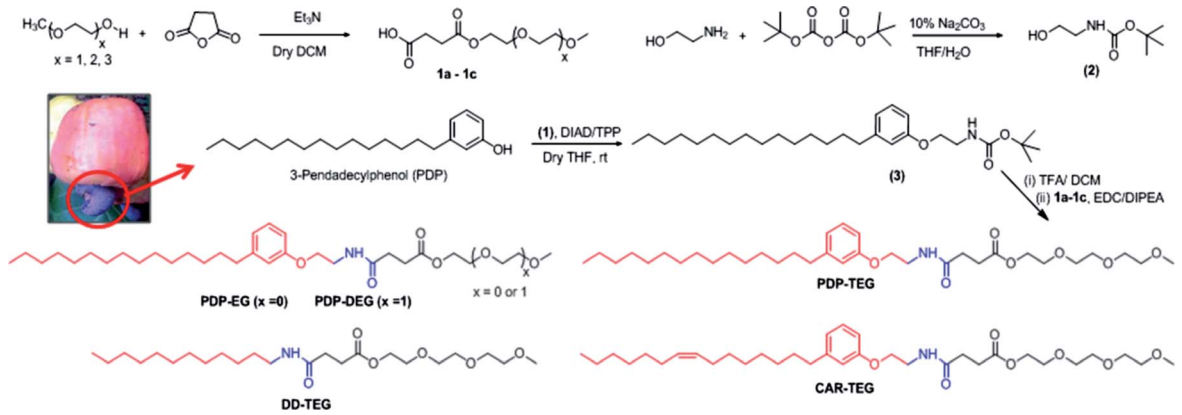

Scheme 1 Synthesis of thermo-responsive amphiphiles.

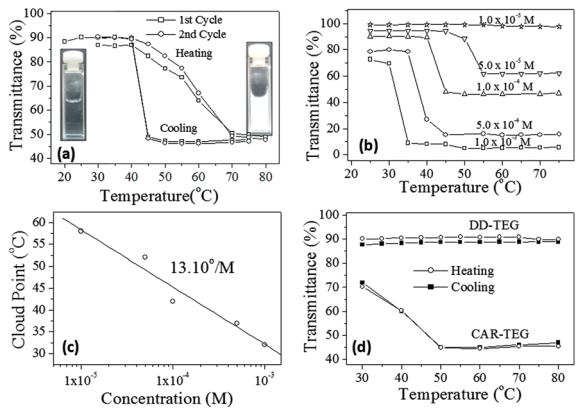

Fig. 2 (a) Temperature dependent optical transmittance of PDP–TEG (10^{-4} M) in water in consecutive heating and cooling cycles. (b) Optical transmittance of PDP–TEG in the cooling cycle for concentrations varying from 10^{-3} M to 10^{-5} M. (c) Plot of the cloud point of PDP–TEG *versus* concentration. (d) Optical transmittance of CAR–TEG and DD–TEG in the heating and cooling cycles (10^{-4} M) in water.

(with an increasing concentration from 10^{-5} M to 10^{-3} M), the cloud point decreased from 56 °C to 32 °C. The slope of the line indicates that the cloud point changes by 13.10° mol^{-1} L^{-1} (or 0.022° g^{-1} L^{-1}) of the amphiphile concentration. The thermo-responsive PNIPAM-copolymer was found to show a cloud point over the concentration range 0.51° g^{-1} L^{-1}.[27] This suggested that the custom designed amphiphile was capable of showing thermo-responsiveness at a much lower concentration (~25 times lower concentration) compared to high molecular weight polymers like PNIPAM. Hence, it may be concluded that PDP–TEG is a potential amphiphilic molecule with a thermo-responsive behaviour equivalent to that of high molecular weight polymers for drug delivery applications.

To study the influence of hydrophobic units on the thermo-responsive behaviour, both DD–TEG and CAR–TEG were investigated and their optical transmittances are shown in Fig. 2d. DD–TEG did not show LCST phenomena while CAR–TEG showed very weak phase-separation. This suggested that the nature of the hydrophobic unit in the amphiphile structure also played a crucial role in the molecular self-assembly. Further, the importance of the amide linkages in the amphiphilic design was also investigated by checking the LCST behaviour for structurally identical amphiphiles having an ester linkage (ester linkage instead of amide, see Fig. S3†).[28] This ester molecule did not show significant LCST behaviour. Thus, an appropriate molecular design is essential to make the small molecular derivatives such as PDP–TEG thermo-responsive amphiphiles. In the present case, the combination of the renewable hydrophobic PDP unit, amide linkages and hydrophilic triethylene glycol monomethyl ether units, provided the appropriate molecular geometry for thermo-responsiveness in PDP–TEG amphiphiles.

Shape and size of the amphiphile self-assembly

To study the thermo-responsive self-organization of the amphiphile in water, PDP–TEG was subjected to variable temperature dynamic light scattering (DLS) and static light scattering (SLS) studies. The DLS histograms of the aggregates

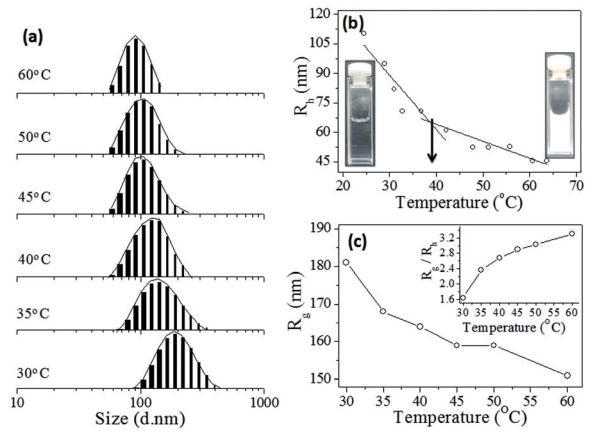

Fig. 3 (a) Variable temperature DLS histograms of PDP–TEG in water at 10^{-4} M. (b) Plot of the hydrodynamic radius *versus* temperature of PDP–TEG. (c) Average radius of gyration (R_g) of PDP–TEG obtained from static light scattering. The inset shows the plot of R_g/R_h *versus* temperature.

Published on 09 April 2014. Downloaded by Florida State University on 21/10/2014 22:57:04.

at different temperatures were measured for a 10^{-4} M solution and their plots are shown in Fig. 3a. PDP–TEG showed monomodal distributions at all the temperatures indicating the formation of homogeneous size aggregates. The stability of these nanoparticles was also investigated in different pH solutions (see Fig. S4†) and it was found that these nanoparticles were stable from the acidic to basic pH of 4.0 to 10.0. The hydrodynamic radius of the aggregates (half of their hydrodynamic diameter) from the DLS were plotted as a function of temperature and shown in Fig. 3b. The figure signified that the hydrodynamic radius of these aggregates decreased with increasing temperature. Below LCST the hydrodynamic radius of these aggregates was 110 ± 10 nm while above LCST it reduced to 45 ± 4 nm. From the plot of R_h *versus* the temperature, the break point was obtained as 40 °C, which is almost identical to the onset temperature for the phase separation (see Fig. 2a). The reversibility of the self-assembly process of the amphiphiles was further investigated by dynamic light scattering techniques (equipped with laser source, excitation 633 nm) for ten consecutive cycles. The amphiphiles showed complete reversibility at temperatures both above and below LCST (see Fig. S5†).

SLS measurements were carried out on a 10^{-4} M solution by heating the sample in a stepwise manner with an interval of 5 °C. The intensity of the scattered light obtained at various angles and at different temperature was then plotted against q^2, where q is the scattering vector magnitude and the plot obtained is known as the Guinier plot (see Fig. S6†). The slope of the Guinier plot gives $(R_g)^{2/3}$, from which the radius of gyration (R_g) was calculated. The plot of the radius of gyration against temperature is shown in Fig. 3c. The plot revealed that with increases in temperature, the radius of gyration decreased from 180 nm to 150 nm. Utilizing the R_g and R_h values obtained at various temperatures from the DLS and SLS measurements, the R_g/R_h ratio was determined (see inset in Fig. 3c). The R_g/R_h increase from 1.6 to ~3.0 as an indication of the transformation from globular to rod-like structures.[29,30]

To visualize the shape and size of the aggregates formed by the amphiphile, the samples were subjected to field emission scanning electron microscopy (FE-SEM), high resolution transmission electron microscopy (HR-TEM), and atomic force microscopy (AFM) analysis. FE-SEM, HR-TEM and AFM images of PDP–TEG at 25 °C (below LCST) are given in Fig. 4. In Fig. 4a, the FE-SEM image of the PDP–TEG shows the existence of spherical core–shell like aggregates with 250 ± 17 nm diameters. The formation of these core–shell structures 255 ± 24 nm in diameter was further confirmed by HR-TEM (see Fig. 4b). The TEM image shows a hollow hydrophobic core surrounded by a hydrophilic shell (dark layer). Further, the AFM image (see Fig. 4e) also shows the existence of 220 ± 20 nm spherical particles. The images of the aggregates above LCST are shown in Fig. 4c, d and f. In Fig. 4c, the aggregates show the formation of clusters instead of isolated particles (as observed below LCST in Fig. 4a). Further, the shape of the aggregates was also transformed from spherical to rod-like structures. The formation of these rod-like nanostructures was further confirmed by HR-TEM image (see Fig. 4d). The internal parts of the rod-like

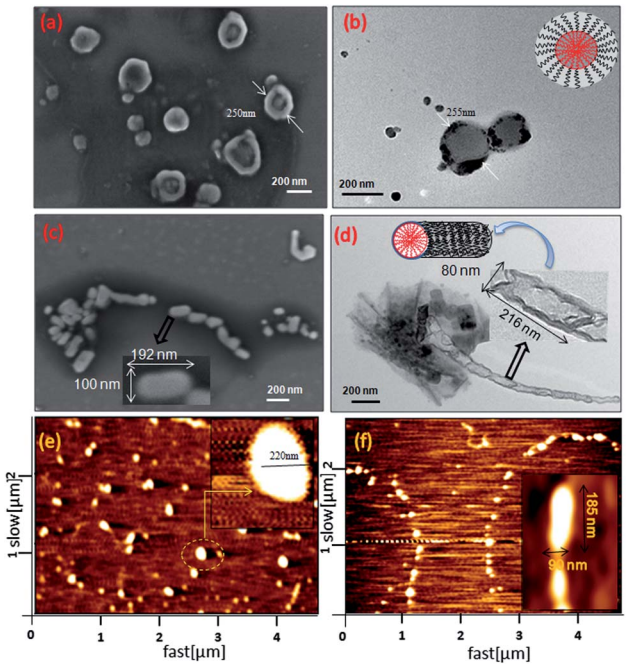

Fig. 4 (a) FE-SEM image of PDP–TEG at 30 °C. (b) HR-TEM image at 30 °C. (c) FE-SEM images of PDP–TEG at 45 °C. (d) TEM images of PDP–TEG at 45 °C. (e) AFM image of PDP–TEG at 30 °C. (f) AFM image of PDP–TEG at 45 °C.

structures were found to be hollow, similarly to the core–shell nanoparticles. AFM images in Fig. 4f also support the formation of elongated structures above LCST. From all three images (Fig. 4c, d and f), it is very clear that the amphiphiles exist as rod-like nanoparticles above LCST and as core–shell nanoparticles below LCST.

To prove the existence of the *in situ* shape transformation in the thermo-responsive scaffolds (see Fig. 5a) in the heating and cooling cycles, the dimensions of the core–shell structures were compared with the rod-like objects. For the above transformation, one would expect the circumference ($2\pi r$, where r = radius of the core–shell) of the spherical core–shell structure to

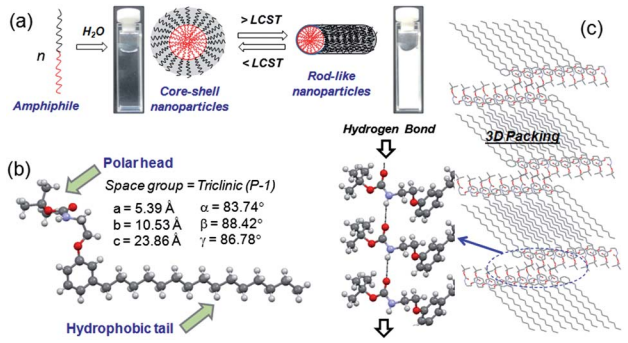

Fig. 5 (a) Mechanism of shape transformation in thermo-responsive scaffolds. (b) Single crystal structure of molecule **3** in Scheme 1. (c) Three dimensional packing of molecule **3** along *a*-axis showing the inter-digitations of the hydrophobic tails and inter-chain hydrogen bonding.

 This journal is © The Royal Society of Chemistry 2014

Published on 09 April 2014. Downloaded by Florida State University on 21/10/2014 22:57:04.

be equal to twice the lengths (L) plus the widths (W) of the nanorods.[31] The average diameter of core–shell nanoparticles was 254 ± 35 nm, 225 ± 40 nm and 183 ± 25 nm from FE-SEM, TEM and AFM, respectively. Thus, the average diameter of the core–shell nanoparticles based on all three techniques together was found to be 220 ± 36 nm (average radius = 110 ± 17 nm). The average diameter of the rod-like structure above LCST was 94 ± 16 nm, 88 ± 18 nm and 108 ± 16 nm from FE-SEM, TEM and AFM, respectively. Likewise, the length of these rod-like structures was 178 ± 37 nm, 193 ± 35 nm and 185 ± 16 nm from FE-SEM, TEM and AFM, respectively. All three techniques together gave a diameter and length of the rod-like structures equal to 97 ± 10 nm and 185 ± 8 nm, respectively. The average circumference of the core–shell structure (below LCST) was calculated as $2\pi r = 0.69 \pm 0.11$ μm. This value matches the $2L + 2D = 0.57 \pm 0.04$ μm of the rod within the experimental error limit. Thus, the average sizes of the rod-like structure were in close agreement with the average diameter of the core–shell nanoparticles. This confirmed that the core–shell nanoparticles collapsed above LCST to produce rod-like structures. The resultant rod-like structures aggregated together to produce a turbid solution above LCST which was completely reversible in the subsequent cooling cycle (see Fig. 2).

The *in situ* shape transition from the hydration (below LCST) to the dehydration (above LCST) state of PDP–TEG was further supported by variable-temperature ^{1}H-NMR studies (see Fig. S7 for more details†). The ^{1}H-NMR spectra of PDP–TEG at various temperatures were recorded in D_2O with an interval of 10 °C from 30 to 70 °C. Below LCST, the signals corresponding to the hydrophobic tail (1.6–0.88 ppm) and aromatic protons (7.18–6.69 ppm) of PDP in the amphiphile appeared with less intensity. This was attributed to the lower exposure of the hydrophobic part of the amphiphile in the aqueous environment in the core–shell state.[32,33] With increase in temperature, the intensity of the signals corresponding to the hydrophobic tail (1.6–0.88 ppm) and aromatic protons (7.18–6.69 ppm) were enhanced. This was attributed to the breaking of the hydrogen bonds of the amide-linkage with water molecules resulting in an increase in chain mobility.[34] These signals showed a complete reversibility in the subsequent cooling cycles. Thus, below LCST, the PDP–TEG amphiphile exist in the form of core–shell nanoparticles. As the temperature was increased above LCST the hydrophilic segments collapsed on the top of the hydrophobic core to produce rod-like assemblies. This type of transition would occur only if the hydrophobic segments are tightly held together in the inner core to facilitate the collapsing or un-coiling of PEG chains at the periphery of the nanoscaffolds.

To provide evidence for the strong packing of the hydrophobic PDP units, the single crystal for compound **3** (see Scheme 1) was obtained in a dichloromethane–methanol solvent mixture (2 : 3 v/v) (for more details see Fig. S8, S9 and ST1 in the ESI†). As it can be seen in Fig. 5b and c, the terminal Boc-protected amine group and the long alkyl tail were arranged in a *trans*-confirmation with respect to each other. The three dimensional packing of the molecules along the *a*-axis showed (see Fig. 5c) that the alkyl chains were extended towards each other *via* hydrophobic–hydrophobic interactions and were inter-digitated. While the enlarged view of the molecular packing (see Fig. 5c) revealed that the molecules were interlocked *via* interchain hydrogen bonding present between the amide linkages of the amphiphiles. Based on the morphology (FE-SEM, HR-TEM and AFM), variable temperature NMR and single crystal structure study, it may be concluded that the newly designed PDP–TEG was a very unique molecule to undergo thermo-responsive phase transition from core–shell to rod-like structures.

Anticancer drug encapsulation

The thermo-responsive amphiphile was further utilized as a scaffold for loading and delivering anticancer drug molecules. Two different hydrophobic anticancer drugs, doxorubicin (DOX) and camptothecin (CPT), were chosen as drug candidates to demonstrate the proof-of-concept of the shape transformable thermo-responsive scaffold. The drugs were encapsulated in the hydrophobic interior of the core–shell particle by the dialysis method. The drug loading content was estimated using absorbance spectroscopy as 4.2 wt% and 1.6 wt% for DOX and CPT, respectively. The sizes of the DOX and CPT loaded scaffolds were determined by DLS and they were found to be 220 ± 20 nm and 190 ± 20 nm, respectively (see Fig. 6a and b). The sizes of the drug loaded particles was similar to that of the nascent ones (see Fig. 3a) indicating that the scaffold retained its self-organization even after the encapsulation of the hydrophobic drugs. The temperature-dependent phase-transition of the DOX and CPT loaded core–shell nanoparticles was investigated and the data are given in Fig. 6c and d. The drug loaded scaffolds preserved the reversible self-organization in the heating cooling cycles similarly to their un-loaded core–shells. The LCST of the DOX encapsulated scaffold was found to be 40 °C which was almost closer to the nascent scaffold (42 °C). On the other hand, the LCST of the CPT loaded scaffolds (see Fig. 6d) was found to be 50 °C which was 8–10° higher than that of the nascent scaffold.

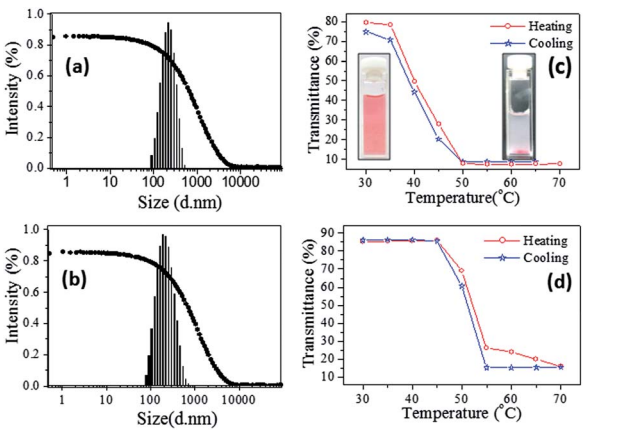

Fig. 6 DLS histogram of DOX (a) and CPT (b) encapsulated scaffolds. Temperature dependence of the transmittance of (c) DOX loaded and (d) CPT loaded PDP–TEG in water at 10^{-4} M.

Published on 09 April 2014. Downloaded by Florida State University on 21/10/2014 22:57:04.

The morphologies of the drug loaded scaffolds are shown in Fig. 7. In the FE-SEM images DOX loaded scaffolds (see Fig. 7a) appear as spherical particles with diameters of 200 ± 10 nm. Above LCST (at 45 °C), the shape of the drug loaded amphiphile underwent morphological transformations from spherical to rod-like structures (see Fig. 7b). These rod-like structures were aggregated together to produce bundles which were arranged in a dendritic fashion (see larger area image Fig. 7c). In Fig. 7d, the TEM images of the DOX loaded scaffolds confirmed the existence of the dendritic nature of the rod-like structures. Though the CPT loaded scaffolds appear as spherical particles having a diameter of 160 ± 10 nm below LCST (see Fig. 6e), they underwent shape transformations into nano-fibrous structures at higher temperatures (see Fig. 7f). These fibrous structures are typically produced by the long range aggregation of the drug plus scaffold. Thus, it may be concluded that the DOX loaded core–shell structures retained the *in situ* phase transitions of nascent scaffolds whereas a long nano-fibrous morphology was obtained for the CPT loaded core–shells.

As both DOX and CPT are fluorescent in nature, the drug loaded nanoparticles were subjected to fluorescence microscopy analysis as well as photophysical studies in order to elucidate their properties in free and encapsulated states. The fluorescence microscopy images of both DOX and CPT loaded nanoparticles are shown in Fig. 7g and h, respectively. Absorbance and emission spectra of free DOX as well as DOX loaded nanoparticles were recorded in water (see Fig. 7i). The absorbance and emission spectra of DOX (see Fig. 7i) did not show any variation upon encapsulation as compared to free DOX.

Similarly, the absorbance and emission spectra of free CPT and CPT loaded scaffolds (see Fig. 7j) were found to be almost identical, which indicated that the properties of CPT did not change upon encapsulation. This was further confirmed by the fluorescence lifetime of the free drug as well as the drug loaded nanoparticles by TCSPC techniques. The decay profile of DOX and CPT in the absence and presence of nanoparticles was collected at 558 nm and 448 nm respectively, using a nano-LED laser source with 460 nm (for DOX) and 347 nm (for CPT) as the excitation wavelength (see Fig. S10 for more details†). The decay profiles were fitted by bi-exponential decay fits using the DAS6 program and their lifetime data are summarized in Table ST2 in the ESI.† The TCSPC lifetime values (τ_1) of DOX upon encapsulation were found to be 1.49 ns, which are in close agreement with the lifetime value of free DOX (0.95 ns). Similarly, lifetime (τ_1) of CPT in loaded as well as free form was 4.66 ns and 4.59 ns, respectively. The DOX and CPT loaded nanoparticles retained their original structural features inside the scaffolds.

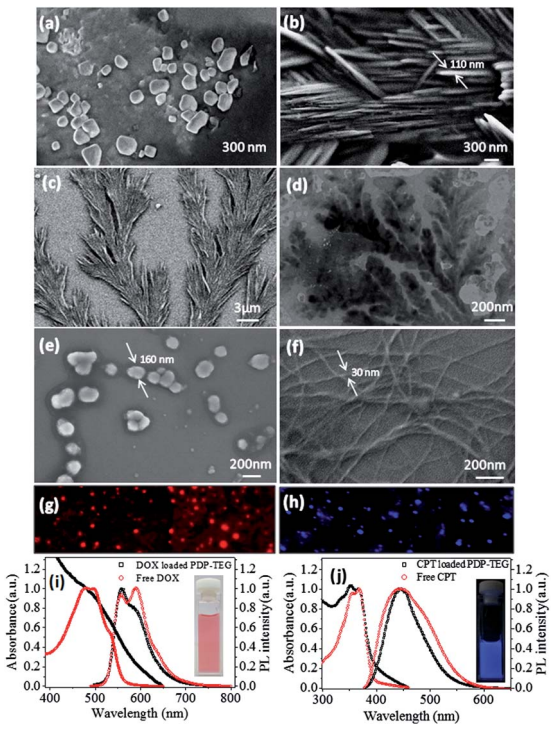

Fig. 7 FE-SEM image of DOX encapsulated PDP–TEG at 30 °C (a), 45 °C (b), and large area image at 45 °C (c) in water at 10^{-4} M. (d) TEM image of DOX encapsulated PDP–TEG at 45 °C in water at 10^{-4} M. FE-SEM image of CPT encapsulated PDP–TEG at 30 °C (e), and 45 °C (f) in water at 10^{-4} M. Fluorescence microscopy images of DOX loaded scaffolds (g), and CPT loaded scaffolds (h) in water at 10^{-4} M. (i) Absorbance and emission spectra of free DOX and DOX loaded scaffolds. (j) Absorbance and emission spectra of free CPT and CPT loaded scaffolds.

In vitro drug release studies

The thermo-responsive drug release of DOX and CPT loaded nanoparticles was studied under physiological conditions (PBS, pH = 7.4) as well as for a cancer tissue environment (PBS, pH = 6.8 see Fig. S11†). It was observed that the release profiles of the drug at pH = 7.4 or pH = 6.8 were identical, indicating that the scaffold was very stable and was also capable of preserving the drug at both pH 6.8 and 7.4. The temperatures for these studies were chosen based on the physiological temperature in cancer tissues (40–43 °C), normal body temperature (37 °C) and drug storage at ambient temperature (25 °C) (see Fig. 1). The drug loaded scaffolds were subjected to incubation at these three different temperatures, *i.e.* 25 °C, 37 °C and 44 °C. The cumulative release profiles of DOX are shown in Fig. 8a. The

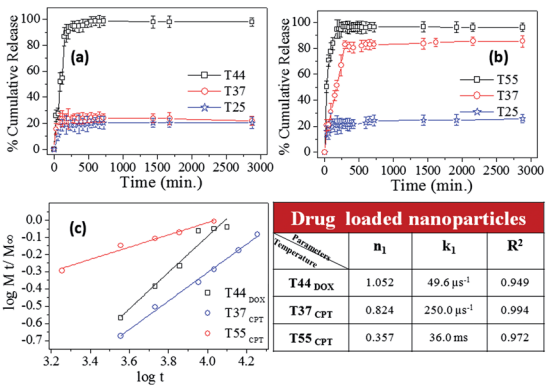

Drug loaded nanoparticles			
Parameters / Temperature	n_1	k_1	R^2
T44 DOX	1.052	49.6 μs^{-1}	0.949
T37 CPT	0.824	250.0 μs^{-1}	0.994
T55 CPT	0.357	36.0 ms	0.972

Fig. 8 Cumulative release profile of (a) DOX and (b) CPT loaded scaffolds. (c) Kinetic plots of DOX and CPT loaded scaffolds. Table contains the values of the rate constant (k) and n of the DOX and CPT releases.

This journal is © The Royal Society of Chemistry 2014

Published on 09 April 2014. Downloaded by Florida State University on 21/10/2014 22:57:04.

percentage release of DOX at temperatures below LCST, *i.e.* 37 °C and 25 °C, was less than 20%. This suggested that the DOX loaded scaffold is very stable both at ambient as well as normal body temperature. At the cancer tissue temperature (above LCST at 44 °C), the DOX loaded scaffold showed a selective release of more than 95% of the drug within 5 h. At 25 °C, the CPT loaded particles (see Fig. 8b) were stable enough, however, at body temperature (37 °C) more than 80% of the drug was released. At temperatures above LCST (55 °C), almost 95% of the drug was released within 5 h. This suggested that the CPT loaded scaffold lost its ability to selectively release the drug at the cancer tissue temperature.

The release of the drug from the polymer matrix involved several processes such as diffusion of the drug from the membrane, erosion of the polymeric scaffolds, and so on. Peppas and co-workers developed a semi-empirical model, as given below, for the drug release:[35]

$$\frac{M_t}{M_\infty} = kt^n \quad (1)$$

$$\log\left(\frac{M_t}{M_\infty}\right) = n \log t + \log k \quad (2)$$

where, M_t and M_∞ are the cumulative amount of drug released at time t and infinite time, respectively, k is a constant that depends on the structural and geometric characteristics of the polymer, and n is the release exponent which indicates the drug release mechanism. In case of spherical particles, the value of $n = 0.43$ for Fickian diffusion and ≥ 0.85 for non-Fickian diffusion. This equation generally holds for the first 60% of the fractional drug release or for values in the interval of $0.1 < M_t/M_\infty < 0.7$. This methodology was adopted by many researchers to study the drug release kinetics for micelles, vesicles and nanogels, and so on. Zhuang and co-workers used the above mentioned equation to study the release mechanism of drug from nanogels,[36] Lecommandoux and co-workers have used the above equation to analyse the release mechanism of drug from polymersomes.[37] The Peppas model was currently employed by Surnar *et al.* from our research group and used the expression to analyse the mode of drug release from polycaprolactone vesicular assemblies.[11,38] In the present investigation, drug release from the thermo-responsive polymer matrix was analysed by the Ritger and Peppas equation and the data are summarized in Fig. 8. The drug release profiles were fitted to the above equation and their kinetics plots log (M_t/M_∞) against log t are shown in Fig. 8c. The rate constant k and n values are reported in the table in Fig. 8. The DOX loaded particles followed non-Fickian diffusion ($n = 1.052$) for selective delivery at the cancer tissue temperature. On the other hand, the CPT loaded scaffold showed an unusual trend in which either non-Fickian diffusion ($n = 0.824$) or Fickian diffusion process ($n = 0.357$) occurs with respect to the normal body and cancer tissue temperatures.

The difference in the release rate of DOX and CPT can be attributed to the difference in their morphology obtained at higher temperatures ($T >$ LCST). The retention of the rod-like structure in the DOX loaded scaffold (similar to nascent one) led to the release of DOX in a controlled manner while the change in the morphology (nan-fibrous structures) in the CPT loaded scaffold results in a burst release. Though, the approach demonstrated here only for two hydrophobic drugs (DOX and CPT), in principle, it is applicable to a wide range of hydrophobic drugs which need to be explored. Thus, the custom designed thermo-responsive amphiphile is a potential candidate for the loading and delivering of anticancer drugs like DOX selectively at the cancer tissue temperature. The current investigation provides for the first time insight into the development of thermo-responsive shape-transformable amphiphilic drug-carriers. The concept was successfully demonstrated based on a new molecular design as well as delivering the anti-cancer drug exclusively at the cancer tissue temperature. The cytotoxicity of the amphiphile and loaded nanoparticles and their cellular uptake mechanism are yet to be studied to confirm their biological activity.

Conclusion

The present investigation demonstrated the design and development of *in situ* shape transformable and thermo-responsive core–shell scaffolds for the first time and established their ability to load and deliver anticancer drug molecules at the cancer tissue temperature. For this purpose, a new amphiphilic molecule consisting of oligoethylene glycols and the renewable resource 3-pentadecyl phenol as the hydrophilic and hydrophobic units, respectively, was custom designed. The amide linkage was used as the self-organization director to facilitate the self-assembly in an aqueous medium with respect to the lower critical solution temperature. The amphiphile self-assembled to produce core–shell nanoparticles at ambient temperature which underwent transformations into one dimensional rod-like assemblies at temperatures closer to the cancer tissue temperature. Dynamic and static light scattering confirmed the occurrence of the *in situ* phase transition with respect to the R_g/R_h ratio. Morphological analysis by FE-SEM, HR-TEM and AFM provided direct evidence for the existence of the amphiphilic core–shell spherical morphology below LCST and rod-like structures above LCST. The shape transformation was further confirmed by carrying out detailed calculations on the circumference of the core–shell and rod-like assemblies. Variable temperature ^{1}H-NMR studies and single crystal structures established the existence of strong inter-digitations among the hydrophobic units which facilitated the thermo-responsive shape transformation. Anticancer drugs, doxorubicin (DOX) and camptothecin (CPT), were successfully loaded into the core–shell nanoparticles. These drug loaded nanoscaffolds retained their thermo-responsive molecular self-organization, similarly to that of their nascent amphiphiles. *In vitro* studies revealed that the DOX loaded scaffolds were very stable at normal body temperature (37 °C) and exclusively collapsed to release more than 90% of the drug at 44 °C, which is similar to that of cancer tissues under physiological conditions. The drug release kinetics indicated that DOX underwent non-Fickian diffusion. Nevertheless, the present investigation provides for the first time insight into the development of *in situ*

Published on 09 April 2014. Downloaded by Florida State University on 21/10/2014 22:57:04.

shape transformable core–shell scaffolds for delivering drugs (like DOX) exclusively at the cancer tissue temperature.

Acknowledgements

The authors thank the research grant from the Department of Science and Technology (DST), New Delhi, India, under nano-mission initiative project SR/NM/NS-42/2009 and the SERB-scheme under the project SB/S1/OC-37/2013. Smita Kashyap thanks CSIR, India for Ph.D. research fellowship. The authors thank HR-TEM facilities and SLS facilities at NCL-Pune.

References

1 E. Fleige, M. A. Quadir and R. Haag, *Adv. Drug Delivery Rev.*, 2012, **64**, 866–884.
2 M. S. Shim and Y. J. Kwon, *Adv. Drug Delivery Rev.*, 2012, **64**, 1046–1049.
3 M. E. Davis, Z. Chen and D. M. Shin, *Nat. Rev. Drug Discovery*, 2008, **7**, 771–782.
4 J. Fang, H. Nakamura and H. Maeda, *Adv. Drug Delivery Rev.*, 2011, **63**, 136–151.
5 K. Maruyama, *Adv. Drug Delivery Rev.*, 2011, **63**, 161–169.
6 Z. Ge and S. Liu, *Chem. Soc. Rev.*, 2013, **42**, 7289–7325.
7 R. D. Issels, *Eur. J. Cancer*, 2008, **44**, 2546–2554.
8 A. E. Felber, M.-H. Dufresne and J.-C. Leroux, *Adv. Drug Delivery Rev.*, 2012, **64**, 979–992.
9 (*a*) Y. Du, W. Chen, M. Zheng, F. Meng and Z. Zhong, *Biomaterials*, 2012, **33**, 7291–7299; (*b*) N. R. Vijayakameswara, S. R. Mane, A. Kishore, J. D. Sarma and R. Shunmugam, *Biomacromolecules*, 2012, **13**, 221–230.
10 (*a*) C. Zhao, P. He, C. Xiao, X. Gao, X. Zhuang and X. Chen, *Adv. Drug Delivery Rev.*, 2011, **359**, 436–442; (*b*) Y. Ding, Z. Wang and X. Zhang, *Chem. Commun.*, 2013, **49**, 5580–5582.
11 B. Surnar and M. Jayakannan, *Biomacromolecules*, 2013, **14**, 4377–4387.
12 (*a*) J. A. Champion and S. Mitragotri, *Pharm. Res.*, 2008, **26**, 244–249; (*b*) S. Venkataraman, J. L. Hedrick, Z. Y. Ong, C. Yang, P. L. R. Ee, P. T. Hammond and Y. Y. Yang, *Adv. Drug Delivery Rev.*, 2011, **63**, 1228–1246.
13 N. Doshi and S. Mitragotri, *Adv. Funct. Mater.*, 2009, **19**, 3843–3854.
14 (*a*) P. Kolhar, N. Doshi and S. Mitragotri, *Small*, 2011, **7**, 2094–2100; (*b*) S. E. A. Gratton, P. A. Ropp, P. D. Pohlhaus, J. C. Luft, V. J. Madden, M. E. Napier and J. M. DeSimone, *Proc. Natl. Acad. Sci. U. S. A.*, 2008, **105**, 11613–11618.
15 Y. Geng, P. Dalhaimer, S. Cai, R. Tsai, M. Tewari, T. Minko and D. E. Denis, *Nat. Nanotechnol.*, 2007, **2**, 249–255.
16 J. A. Champion and S. Mitragotri, *Proc. Natl. Acad. Sci. U. S. A.*, 2006, **103**, 4930–4934.
17 (*a*) M. E. Fox, F. C. Szoka and J. M. Frechet, *Acc. Chem. Res.*, 2009, **42**, 1141–1151; (*b*) B. Chen, K. Jerger, J. M. J. Frechet and F. C. Szoka Jr, *J. Controlled Release*, 2009, **140**, 203–209.
18 S. Stolnik, L. Illum and S. S. Davis, *Adv. Drug Delivery Rev.*, 1995, **16**, 195–214.
19 Z. Ge and S. Liu, *Chem. Soc. Rev.*, 2013, **42**, 7289–7325.
20 S. Mura, J. Nicholas and P. Couvreur, *Nat. Mater.*, 2013, **12**, 991–1003.
21 H. Wei, X. Zhang, C. Cheng, S.-X. Cheng and R.-X. Zhuo, *Biomaterials*, 2007, **28**, 99–107.
22 Y. Y. Li, X. Z. Zhang, J. L. Zhu, H. Cheng, S. X. Cheng and R. X. Zhuo, *Nanotechnology*, 2007, **18**, 215605–215612.
23 S. Q. Liu, Y. W. Tong and Y.-Y. Yang, *Biomaterials*, 2005, **26**, 5064–5074.
24 D.-H. Kim, E. A. Vitol, J. Liu, S. Balasubramanian, D. J. Gosztola, E. E. Cohen, V. Novosad and E. A. Rozhkova, *Langmuir*, 2013, **29**, 7425–7432.
25 H. Chen, B. Li, J. Qiu, J. Li, J. Jin, S. Dai, Y. Ma and Y. Gu, *Nanoscale*, 2013, **5**, 12409–12424.
26 (*a*) J. Ding, L. Zhao, D. Li, C. Xiao, X. Zhuang and X. Chen, *Polym. Chem.*, 2013, **4**, 3345–3356; (*b*) J. Ding, F. Shi, C. Xiao, L. Lin, L. Chen, C. He, X. Zhuang and X. Chen, *Polym. Chem.*, 2011, **2**, 2857–2864; (*c*) F. Shi, J. Ding, C. Xiao, X. Zhuang, C. He, L. Chen and X. Chen, *J. Mater. Chem.*, 2012, **22**, 14168–14179.
27 P. J. Roth, T. P. Davis and A. B. Lowe, *Macromolecules*, 2012, **45**, 3221–3230.
28 S. Kashyap and M. Jayakannan, *J. Phys. Chem. B*, 2012, **116**, 9820–9831.
29 (*a*) R. G. Alargova, K. D. Danov, P. A. Kralchevsky, G. Broze and A. Mehreteab, *Langmuir*, 1998, **14**, 4036–4049; (*b*) J. R. Mishic and M. R. Fisch, *J. Chem. Phys.*, 1990, **92**, 3222–3229.
30 B. Herzog, K. Huber and A. R. Rennie, *J. Colloid Interface Sci.*, 1994, **164**, 370–381.
31 P. Anilkumar and M. Jayakannan, *J. Phys. Chem. B*, 2009, **113**, 11614–11624.
32 F. Cau and S. Lacelle, *Macromolecules*, 1996, **29**, 170–178.
33 (*a*) J.-H. Ma, C. Guo, Y.-L. Tang and H.-Z. Liu, *Langmuir*, 2007, **23**, 9596–9605; (*b*) J. Weiss, C. Bottcher and A. Laschewsky, *Soft Matter*, 2011, **7**, 483–492.
34 (*a*) J. S. Hrkach, M. T. Peracchia, A. Domb, N. Lotan and R. Langer, *Biomaterials*, 1997, **18**, 27–30; (*b*) Y. Li, S. Pan, W. Zhang and Z. Du, *Nanotechnology*, 2009, **20**, 1–11.
35 (*a*) J. Siepmann and N. A. Peppas, *Adv. Drug Delivery Rev.*, 2001, **48**, 139–157; (*b*) C. R. Young, C. Dietzsch, M. Cerea, T. Farrell, K. A. Fegley, A. Rajabi-Siahboomi and J. W. Mcginity, *Int. J. Pharm.*, 2005, **301**, 112–120.
36 F. Shi, J. Ding, C. Xiao, X. Zhuang, C. He, L. Chen and X. Chen, *J. Mater. Chem.*, 2012, **22**, 14168–14179.
37 C. Sanson, C. Schatz, J.-F. L. Meins, A. Soum, J. Thevenot, E. Garanger and S. Lecommandoux, *J. Controlled Release*, 2010, **147**, 428–435.
38 B. Surnar, P. S. Subash and M. Jayakannan, *Z. Anorg. Allg. Chem.*, 2014, DOI: 10.1002/zaac.201400030.

 This journal is © The Royal Society of Chemistry 2014